

# Optimal Dynamic Ancillary Services Provision Based on Local Power Grid Perception

Verena Häberle, *Graduate Student Member, IEEE*, Xiuqiang He, *Member, IEEE*, Linbin Huang, *Member, IEEE*, Eduardo Prieto-Araujo, *Senior Member, IEEE*, and Florian Dörfler, *Senior Member, IEEE*

**Abstract**—In this paper, we propose a systematic closed-loop approach to provide optimal dynamic ancillary services with converter-interfaced generation systems based on local power grid perception. In particular, we structurally encode dynamic ancillary services such as fast frequency and voltage regulation in the form of a *parametric transfer function matrix*, which includes several parameters to define a set of different feasible response behaviors, among which we aim to find the optimal one to be realized by the converter system. Our approach is based on a so-called “*perceive-and-optimize*” (P&O) strategy: First, we identify a grid dynamic equivalent at the interconnection terminals of the converter system. Second, we consider the closed-loop interconnection of the identified grid equivalent and the parametric transfer function matrix, which we optimize for the set of transfer function parameters, resulting in a stable and optimal closed-loop performance for ancillary services provision. In the process, we ensure that grid-code and device-level requirements are satisfied. Finally, we demonstrate the effectiveness of our approach in different numerical case studies based on a modified Kundur two-area test system.

## I. INTRODUCTION

TODAY’S grid-code specifications for dynamic ancillary services provision (e.g., fast frequency and voltage regulation) with converter-based generation units are typically defined by a prescribed time-domain step-response characteristic [1]–[4]. As an example, the European network code [1], which is adopted in most European national grid codes, specifies the active power provision for frequency containment reserve (FCR) in response to a frequency step change by a piecewise linear time-domain curve (Fig. 2a). Likewise, the dynamic response of reactive power for voltage regulation is defined via time-domain specifications in response to a voltage step change [1]. Recent grid codes (e.g., Finland [2], Ireland [3], Sweden/Norway/Denmark [4]) also define the activation of fast frequency reserves (FFR) or synthetic inertia response via piecewise linear active power curves in the time domain. Such grid codes are used to involve power converters in supporting low-inertia power grids and are important measures to ensure the transition toward converter-dominated power systems.

Although the specification of the piecewise linear time-domain curves in today’s grid codes is straightforward, they only assign the lower bound of the *open-loop* response characteristic for an ancillary services-providing reserve unit (see, e.g., Fig. 2a). On the one hand, different dynamic responses of a

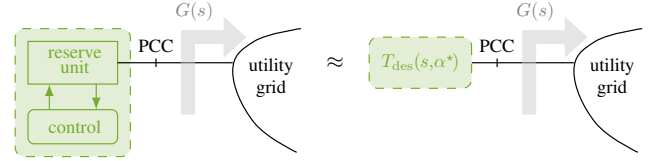


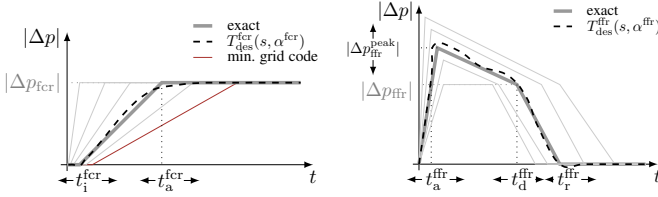
Figure 1: Sketch of a grid-connected reserve unit to provide closed-loop optimal dynamic ancillary services in the form of a desired rational transfer function matrix  $T_{\text{des}}(s, \alpha^*)$ . The grid dynamic equivalent is represented by  $G(s)$ .

reserve unit are allowed, as long as the grid-code requirements are satisfied at or above the piece-wise linear curves. This results in a family of different feasible response behaviors, where the reserve unit injection is often pared down to the minimum by just satisfying the grid-code requirements at its boundaries. On the other hand, the current grid-code specifications are *indistinguishable* for any location of converter-interfaced generation, regardless of the grid strength and dynamic characteristics at the grid-connection point. However, in future power systems with increased penetration of converter-based generation, such indistinguishable grid-code specifications in an open-loop manner will result in a sub-optimal closed-loop power system response with poor dynamic performance or even unstable behaviors [5], [6]. In this regard, existing studies in [7]–[9] have indicated that the location of synthetic inertia and damping should be carefully chosen to provide better stability and dynamic performance. Therefore, future grid-code specifications for dynamic ancillary services provision may have to respect distinguishably the local grid dynamic characteristics in a closed-loop manner.

Moreover, beyond the flaw of specifying an open-loop response characteristic and being indistinguishable for any power grid condition, the practical implementation of the piece-wise linear time-domain grid-code curves in converters is not immediate, and no systematic methods have been developed yet. In this regard, today’s industrial practice is often ad-hoc and highly customized, e.g., relying on open-loop trajectory commands [10], varying gains [11], [12], or look-up table schemes to approximately satisfy the grid codes. The design, implementation, and tuning of such methods, however, are in general time-consuming and rigid, which impedes its applicability.

To overcome the previous shortcomings, we propose a *closed-loop* approach to provide *optimal* dynamic ancillary services based on *local* power grid perception, which systematically ensures that open-loop grid code requirements and device-level limitations are reliably satisfied. To be specific, we translate the aforementioned time-domain grid-code capability curves into a rational parametric transfer function matrix  $T_{\text{des}}(s, \alpha)$  in the frequency domain, which defines a tractable desired response behavior to be realized by the converter (see Fig. 1). The parameter vector  $\alpha$  establishes a set of feasible response behaviors

This work was supported by the European Union’s Horizon 2020 and 2023 research and innovation programs (Grant Agreement Numbers 883985 and 101096197). Verena Häberle, Xiuqiang He, Linbin Huang and Florian Dörfler are with the Automatic Control Laboratory, ETH Zurich, 8092 Zurich, Switzerland. Email: {verenhae,xiuqhe,linhuang,dorfler}@ethz.ch. Eduardo Prieto-Araujo is a Serra Hünter Lecturer with CITCEA, Department d’Enginyeria Elèctrica, Universitat Politècnica de Catalunya, 08028 Barcelona, Spain. Email: eduardo.prieto-araujo@upc.edu



(a) Exemplary active power time-domain capability curve for FCR provision after a frequency step change [1]: the reserve unit has to deliver a certain FCR capacity  $|\Delta p_{fcr}|$  in accordance with an initial delay time  $t_i^{fcr}$  and a full activation time  $t_a^{fcr}$ , where the FCR capacity  $|\Delta p_{fcr}|$  is typically fixed by the allocated active power droop gain  $D_p$  and the amplitude of the frequency step input  $\Delta f$ , i.e.,  $|\Delta p_{fcr}| = |\frac{1}{D_p} \Delta f|$ . The minimum grid-code curve requirements are exemplarily indicated in red.

(b) Exemplary active power time-domain capability curve for FFR provision after a frequency step change [2]: the reserve unit has to deliver the FFR capacity  $|\Delta p_{ffr}|$  after an activation time  $t_a^{ffr}$ , which has to remain activated until a particular support duration time  $t_d^{ffr}$ , before returning to recovery at time  $t_r^{ffr}$ . The overdelivery  $|\Delta p_{ffr}^{peak}|$  is a multiple of the FFR capacity, i.e.,  $|\Delta p_{ffr}^{peak}| = x^{ffr} |\Delta p_{ffr}|$ , where  $|\Delta p_{ffr}|$  is defined by the scaled amplitude of the frequency step input, i.e.,  $|\Delta p_{ffr}| = |\frac{1}{K_p} \Delta f|$ .

Figure 2: Examples of piece-wise linear time-domain grid-code curves (simplified) and their approximation as rational parametric transfer functions.

constrained by the grid-code and device-level limitations, out of which we aim to find the optimal behavior such that a stable and optimal closed-loop performance of the entire power system can be achieved. To do so, our approach is based on a so-called “*perceive-and-optimize*” (P&O) strategy, which is composed of two main steps: We first use the converter-based reserve unit to identify a grid dynamic equivalent  $G(s)$  at its interconnection terminals (“*perceive*”). Second, we consider the closed-loop interconnection of the identified grid dynamic equivalent  $G(s)$  and the converter (represented by the parametric transfer function matrix  $T_{des}(s, \alpha)$ ), where we optimize  $\alpha$  to achieve an optimal and stable closed-loop performance of the entire power grid response, while ensuring grid-code and device-level requirements to be reliably satisfied (“*optimize*”).

Numerous studies have explored the optimization of dynamic ancillary services provision, as evidenced by works such as [7], [8]. These endeavors invariably rely on precise knowledge of the dynamic power system model or its approximation, which, however, is typically unavailable in practice. Moreover, these methods failed to consider potential variations in grid conditions over time. Conversely, alternative approaches, exemplified by [13], proposed adaptive tuning methods to enhance the dynamic response behavior of grid-connected converter systems based on local power grid measurements, thereby taking a similar P&O perspective as proposed in our work. Despite its innovation, however, the suggested concept in [13] is highly specialized and confined to providing power oscillation damping services, lacking immediate adaptability to other dynamic ancillary service products. Notably, none of the methods outlined in [7], [8], [13] account for grid-code or device-level requirements. This stands in vast contrast to our method for optimal dynamic ancillary services provision, characterized by its ability to:

- perceive *local* grid dynamics,
- attain optimal performance in a *closed loop* with the grid,
- encode *grid-code* and *device-level requirements*,
- accommodate *time-varying grid conditions*, and
- offer a *systematic* and *versatile* approach applicable to a wide range of dynamic ancillary services products.

The remainder of this paper is structured as follows. In Section II we demonstrate how to encode dynamic ancillary services as a parametric transfer function  $T_{des}(s, \alpha)$ . In Section III, we present the novel P&O strategy for optimal dynamic ancillary services provision, including the grid dynamic equivalent identification, and the optimization problem to compute the optimal parameter vector  $\alpha^*$  of the transfer function matrix  $T_{des}(s, \alpha)$ . In Section IV, we provide numerical case studies to demonstrate the vastly superior performance of our approach over only fulfilling the minimum (open-loop) grid-code requirements. Section V concludes the paper.

## II. ENCODING DYNAMIC ANCILLARY SERVICES AS PARAMETRIC TRANSFER FUNCTIONS

We consider dynamic ancillary services to be encoded in the form of a rational parametric transfer function matrix  $T_{des}(s, \alpha)$  in the frequency domain (with parameter vector  $\alpha = [\alpha^{fp}, \alpha^{vq}]$ ), specifying a *desired* decoupled frequency and voltage control behavior to be realized by a reserve unit, i.e.,

$$\begin{bmatrix} \Delta p(s) \\ \Delta q(s) \end{bmatrix} = \underbrace{\begin{bmatrix} T_{des}^{fp}(s, \alpha^{fp}) & 0 \\ 0 & T_{des}^{vq}(s, \alpha^{vq}) \end{bmatrix}}_{= T_{des}(s, \alpha)} \begin{bmatrix} \Delta f(s) \\ \Delta v(s) \end{bmatrix}, \quad (1)$$

where  $\Delta f$  and  $\Delta v$  are the measured bus frequency and voltage magnitude deviation, and  $\Delta p$  and  $\Delta q$  the active and reactive power output deviations (deviating from the respective power set point). In particular, the transfer function matrix in (1) defines a tractable response behavior which can be easily realized in standard converter control architectures as a reference model to be matched. Inspired by today’s grid-code specifications for transmission networks, we stick to a classical decoupled grid-following frequency and voltage regulation in (1). However, our formalism directly extends to fully coupled multi-input multi-output specifications for  $T_{des}(s, \alpha)$ , potentially relevant for future ancillary services or in other types of networks [14]. Moreover, also grid-forming implementations with inverse signal causality can be considered [15].

The transfer functions in (1) are defined as a superposition of different dynamic ancillary services products  $T_{des}^{fp,i}(s, \alpha^{fp,i})$  and  $T_{des}^{vq,i}(s, \alpha^{vq,i})$  (acting on different time-scales [16]), i.e.,

$$T_{des}^{fp}(s, \alpha^{fp}) = \sum_i T_{des}^{fp,i}(s, \alpha^{fp,i}), \quad (2a)$$

$$T_{des}^{vq}(s, \alpha^{vq}) = \sum_i T_{des}^{vq,i}(s, \alpha^{vq,i}). \quad (2b)$$

where the parametric structure of  $T_{des}^{fp,i}(s, \alpha^{fp,i})$  and  $T_{des}^{vq,i}(s, \alpha^{vq,i})$  results from the different grid-code requirements of each dynamic ancillary services product  $i$ , as detailed below.

### A. Frequency Regulation

Nowadays, typical dynamic ancillary service products for frequency regulation are *frequency containment reserve (FCR)* [1], *fast frequency response (FFR)* [2]–[4], and *other auxiliary controls such as power oscillation damping (POD)* [1], [17]. In this regard, we can specify  $T_{des}^{fp}(s, \alpha^{fp})$  in (2a) as

$$T_{des}^{fp}(s, \alpha^{fp}) = T_{des}^{fcr}(s, \alpha^{fcr}) + T_{des}^{ffr}(s, \alpha^{ffr}) + T_{des}^{aux}(s, \alpha^{aux}), \quad (3)$$

where  $T_{des}^{fcr}(s, \alpha^{fcr})$  encodes the FCR provision,  $T_{des}^{ffr}(s, \alpha^{ffr})$  the FFR provision, and  $T_{des}^{aux}(s, \alpha^{aux})$  defines an auxiliary service

to improve fast dynamics and grid oscillations such as POD. Of course, depending on the requirements of different grid codes, one might consider also other types of dynamic ancillary service products. However, for the sake of simplicity, we stick to the products in (3), which are common in practice.

The structure and parameters of the transfer function terms in (3) can be obtained from the underlying grid-code specification of each ancillary service product. For instance, in the case of the FCR and FFR provision, the associated grid-code specifications are typically defined by some prescribed piece-wise linear time-domain curves (Fig. 2), where the required active power response should be satisfied at or above some minimum requirements. By applying our recent method in [18] (which is based on Laplace transformations followed by Padé approximations of appropriate order), we can translate such piece-wise linear time-domain curves into the aforementioned rational parametric transfer functions  $T_{\text{des}}^{\text{fcr}}(s, \alpha^{\text{fcr}})$  and  $T_{\text{des}}^{\text{ffr}}(s, \alpha^{\text{ffr}})$  in the frequency domain, respectively. The parameter vector  $\alpha$  used in these transfer functions contains the parameters of the time-domain curves, which have to satisfy certain grid-code and device-level requirements.

As an example, for the parameters  $\alpha^{\text{fcr}} := [t_i^{\text{fcr}}, t_a^{\text{fcr}}]$  of the FCR curve in Fig. 2a, we require [1]

$$0 \leq t_i^{\text{fcr}} \leq t_{i,\text{max}}^{\text{fcr}} \quad (4a)$$

$$t_i^{\text{fcr}} \leq t_a^{\text{fcr}} \leq t_{a,\text{max}}^{\text{fcr}} \quad (4b)$$

$$|\Delta p_{\text{fcr}}| \leq (t_a^{\text{fcr}} - t_i^{\text{fcr}}) \cdot r_{\text{max}}^{\text{p}}, \quad (4c)$$

where  $t_{i,\text{max}}^{\text{fcr}}$  and  $t_{a,\text{max}}^{\text{fcr}}$  are the maximum admissible FCR initial delay and activation times, and  $r_{\text{max}}^{\text{p}}$  is the maximal active power ramping rate of the reserve unit, as specified in Table I and graphically illustrated by the minimum curve requirement (red) in Fig. 2a. Hence, as indicated by the family of light gray curves in Fig. 2a, the requirements in (4) establish a set of different feasible response behaviors for the reserve unit. For a particular feasible  $\alpha^{\text{fcr}}$  as for the bold gray curve in Fig. 2a, the unit step response of the associated translated transfer function  $T_{\text{des}}^{\text{fcr}}(s, \alpha^{\text{fcr}})$  is exemplarily indicated by the black dashed line. Finally, the requirements (4) can be divided into grid-code and device-level specifications as

$$\alpha^{\text{fcr}} \in \mathcal{G}^{\text{fcr}} \cap \mathcal{D}^{\text{fcr}}, \quad (5)$$

where the grid-code specification set  $\mathcal{G}^{\text{fcr}}$  is defined by the constraints in (4a) and (4b), and the device-level limitation set  $\mathcal{D}^{\text{fcr}}$  by the constraint in (4c), respectively.

Likewise, also the parameters  $\alpha^{\text{ffr}} := [t_a^{\text{ffr}}, t_d^{\text{ffr}}, t_r^{\text{ffr}}, x^{\text{ffr}}]$  of the FFR curve in Fig. 2b are subject to grid-code and device-level constraints similar to (4), i.e.,

$$\alpha^{\text{ffr}} \in \mathcal{G}^{\text{ffr}} \cap \mathcal{D}^{\text{ffr}}, \quad (6)$$

where the grid-code and device-level constraint sets  $\mathcal{G}^{\text{ffr}}$  and  $\mathcal{D}^{\text{ffr}}$  encode several time and capacity bounds as listed in Table I, which establish a feasible set of response behaviors as illustrated by the family of light gray curves in Fig. 2b. A detailed formulation of (6) can be found in the grid-code documents [2]–[4] or more compactly in our recent work [18].

In contrast to the FCR and FFR grid-code specifications, the damping of high-frequency dynamics and/or power oscillations is usually stated less specifically in today's grid codes, despite

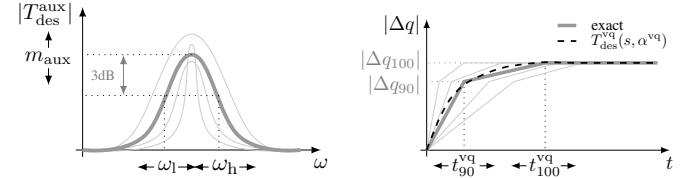
Table I: Grid-code and device-level specification examples.

(a) Grid-code specifications (exemplary values adopted from [1]–[3], [17]).

Parameter	Symbol	Value
Maximum admissible initial delay time for FCR	$t_{i,\text{max}}^{\text{fcr}}$	2 s
Maximum admissible full activation time for FCR	$t_{a,\text{max}}^{\text{fcr}}$	30 s
Maximum admissible full activation time for FFR	$t_{a,\text{max}}^{\text{ffr}}$	2 s
Minimum support duration time for FFR	$t_{d,\text{min}}^{\text{ffr}}$	$8 \text{ s} + t_{a,\text{max}}^{\text{ffr}}$
Minimum return-to-recovery time for FFR	$t_{r,\text{min}}^{\text{ffr}}$	$10 \text{ s} + t_{d,\text{min}}^{\text{ffr}}$
Maximum overdelivery factor during FFR	$x_{\text{max}}^{\text{ffr}}$	1.35
Minimum frequency for oscillation damping	$\omega_{\text{min}}$	$2\pi \cdot 0.1 \frac{\text{rad}}{\text{s}}$
Maximum frequency for oscillation damping	$\omega_{\text{max}}$	$2\pi \cdot 3 \frac{\text{rad}}{\text{s}}$
Maximum admissible 90% reactive power activation time	$t_{90,\text{max}}^{\text{vq}}$	5 s
Maximum admissible 100% reactive power activation time	$t_{100,\text{max}}^{\text{vq}}$	60 s

(b) Device-level specifications (values depend on the reserve unit).

Parameter	Symbol
Maximum active power ramping rate of reserve unit	$r_{\text{max}}^{\text{p}} = R_{\text{max}}^{\text{p}} \Delta f_{\text{max}}$
Maximum reactive power ramping rate of reserve unit	$r_{\text{max}}^{\text{q}} = R_{\text{max}}^{\text{q}} \Delta v_{\text{max}}$
Maximum active power peak capacity of reserve unit	$m_{\text{max}}^{\text{p}} = M_{\text{max}}^{\text{p}} \Delta f_{\text{max}}$
Maximum FFR support duration time of reserve unit	$t_{\text{d,max}}^{\text{ffr}}$
Maximum FFR return-to-recovery time of reserve unit	$t_{\text{r,max}}^{\text{ffr}}$



(a) Exemplary magnitude Bode plot of bandpass resonator transfer function for active power oscillation damping:  $\omega_r = \sqrt{\omega_l \omega_h}$  is the resonance frequency,  $\Delta \omega_{\text{BW}} = \omega_h - \omega_l$  the filter bandwidth, and  $m_{\text{aux}}$  the magnitude.

(b) Exemplary reactive power time-domain capability curve for voltage control after a voltage step change [1]: the reserve unit has to deliver the reactive power capacity levels  $|\Delta q_{90}|$  of 90% and  $|\Delta q_{100}|$  of 100% in accordance with the times  $t_{90}^{\text{vq}}$  and  $t_{100}^{\text{vq}}$ , respectively, where the reactive power capacity levels  $|\Delta q_{90}|$  and  $|\Delta q_{100}|$  are typically fixed by the allocated reactive power droop gain  $D_q$  and the amplitude of the voltage step input  $\Delta v$ , i.e.,  $|\Delta q_{100}| = |\frac{1}{D_q} \Delta v|$ .

Figure 3: Examples of dynamic ancillary services products (simplified) encoded as rational parametric transfer functions.

its importance for grid-connected converters to provide damping services, similar to the PSS in synchronous generators [1]. Note that grid codes often only specify a certain range of frequencies  $[\omega_{\text{min}}, \omega_{\text{max}}]$  in which the POD service has to be provided (e.g., Spain [17]), without prescribing a particular response behavior for the reserve unit. In respect thereof, we define the parametric structure of  $T_{\text{des}}^{\text{aux}}(s, \alpha^{\text{aux}})$  in the form of a bandpass resonator transfer function as in Fig. 3a, i.e.,

$$T_{\text{des}}^{\text{aux}}(s, \alpha^{\text{aux}}) = m_{\text{aux}} \cdot \frac{(\omega_h - \omega_l)s}{s^2 + (\omega_h - \omega_l)s + \omega_l \omega_h}, \quad (7)$$

where the parameters  $\alpha^{\text{aux}} = [\omega_l, \omega_h, m_{\text{aux}}]$  have to satisfy grid-code and device-level constraints compactly denoted as

$$\alpha^{\text{aux}} \in \mathcal{G}^{\text{aux}} \cap \mathcal{D}^{\text{aux}}. \quad (8)$$

In particular, the grid-code specification set  $\mathcal{G}^{\text{aux}}$  is defined by the frequency range  $[\omega_{\text{min}}, \omega_{\text{max}}]$  to damp high-frequency dynamics and/or power oscillations, and the device-level limitation set  $\mathcal{D}^{\text{aux}}$  limits the resonance amplitude according to the reserve unit's maximum capacity (see Table I), thereby establishing a feasible set of different resonator transfer functions as indicated by the light gray curves in Fig. 3a.

Finally, by superimposing the previous transfer functions, we can establish the overall frequency control specification  $T_{\text{des}}^{\text{fp}}(s, \alpha^{\text{fp}})$  as in (3). In doing so, we further need to ensure that the maximum capacity and bandwidth limitations of the reserve unit are not violated during a *superimposed* injection of active power. We encode these overarching constraints via an additional overall device-level constraint set  $\mathcal{D}^{\text{fp}}$  for f-p control.

### B. Voltage Regulation

In analogy to the frequency regulation, we in general also consider  $T_{\text{des}}^{\text{vq}}(s, \alpha^{\text{vq}})$  in (2b) as a superposition of different voltage regulation products. The most common and often even only specified voltage control service in today's grid codes is the dynamic activation of reactive power proportionately to a voltage step change under particular time specifications [1]. An example of the associated piece-wise linear grid-code curve is shown in Fig. 3b, and the associated translated transfer function response is indicated via black dashed lines. Notice that the voltage control provision in Fig. 3b might be specified differently in different grid codes. Moreover, in the same vein as for frequency regulation, one might also further populate the voltage regulation transfer function  $T_{\text{des}}^{\text{vq}}(s, \alpha^{\text{vq}})$  with some additional auxiliary term(s) for oscillation damping, etc.

The time-parameters  $\alpha^{\text{vq}} := [t_{90}^{\text{vq}}, t_{100}^{\text{vq}}]$  for the reactive power curve example in Fig. 3b have to satisfy grid-code and device level requirements similar to (4) as

$$\alpha^{\text{vq}} \in \mathcal{G}^{\text{vq}} \cap \mathcal{D}^{\text{vq}}, \quad (9)$$

where the grid-code and device-level constraint sets  $\mathcal{G}^{\text{vq}}$  and  $\mathcal{D}^{\text{vq}}$  encode several time constraints as listed in Table I. A detailed formulation of (9) can be found in the associated grid-code document [1] or more compactly in our recent work [18].

Ultimately, by putting all ancillary service products together, we can establish the desired parametric transfer function matrix  $T_{\text{des}}(s, \alpha)$  with parameter vector  $\alpha = [\alpha^{\text{fp}}, \alpha^{\text{vq}}] \in \mathbb{R}^n$  in (1), where  $\alpha^{\text{fp}} := [\alpha^{\text{fcr}}, \alpha^{\text{ffr}}, \alpha^{\text{aux}}]$ , to encode a set of feasible response behaviors for dynamic ancillary services provision. Out of the latter, we aim to find the optimal behavior  $T_{\text{des}}(s, \alpha^*)$  as elaborated in the next section. It should be emphasized that our goal is to do more than cheaply satisfy the minimum open-loop grid-code requirements (e.g., by choosing  $\alpha$  as the critical point where all grid-code constraints are active), with the ultimate goal being an optimal closed-loop performance regardless of the characteristics of the power grid.

### III. OPTIMAL DYNAMIC ANCILLARY SERVICES PROVISION

We abstract the circuit topology in Fig. 1 and consider now a small-signal block diagram for the closed-loop interconnection of the grid dynamic equivalent  $G(s)$  and the rational parametric transfer function matrix  $T_{\text{des}}(s, \alpha)$  for dynamic ancillary services provision as depicted in Fig. 4.

The  $2 \times 2$  transfer function matrix  $T_{\text{des}}(s, \alpha)$  in (1) encodes a decoupled frequency and voltage control and relies on a grid-following signal causality, where the active and reactive power injection changes  $\Delta p$  and  $\Delta q$  are controlled as a function of the frequency and voltage magnitude measurements  $\Delta f$  and  $\Delta v$ . In line with that, we approximate the power grid at the interconnection terminals of the reserve unit, i.e., the

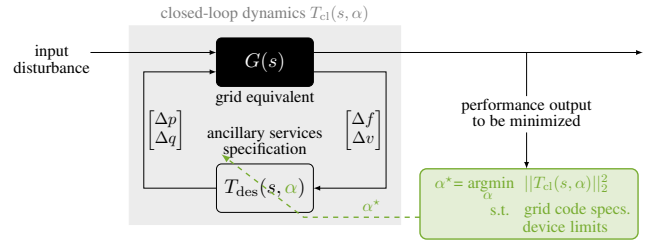


Figure 4: Closed-loop interconnection of the grid dynamic equivalent  $G(s)$  with the rational parametric transfer function matrix  $T_{\text{des}}(s, \alpha)$  which is optimized for dynamic ancillary services provision.

point of common coupling (PCC), by a  $2 \times 2$  small-signal dynamic equivalent  $G(s)$ , which describes the linearized power grid dynamics at the current steady-state operating point, and establishes the bus frequency and voltage magnitude deviations in response to the active and reactive power injections, i.e.,

$$\begin{bmatrix} \Delta f(s) \\ \Delta v(s) \end{bmatrix} = \underbrace{\begin{bmatrix} G_{11}(s) & G_{12}(s) \\ G_{21}(s) & G_{22}(s) \end{bmatrix}}_{=:G(s)} \begin{bmatrix} \Delta p(s) \\ \Delta q(s) \end{bmatrix}. \quad (10)$$

Since the dynamic model of the power system is typically not available in practice, we will identify the grid dynamic equivalent  $G(s)$  in (10) from data, which is outlined in the following subsection.

In this paper, we aim to compute the optimal parameter vector  $\alpha^*$  of the desired transfer function matrix  $T_{\text{des}}(s, \alpha^*)$  which ensures an optimal and stable closed-loop performance of the interconnection in Fig. 4, while simultaneously satisfying (open-loop) grid-code and device-level requirements. Our approach is based on a so-called “*perceive-and-optimize*” (P&O) strategy, which is composed of two main steps (see flow-chart in Fig. 5) and elaborated in the following subsections, i.e.,

- 1) “*Perceive:*” We first use the converter-based reserve unit to identify a grid dynamic equivalent  $G(s)$  at its interconnection terminals.
- 2) “*Optimize:*” We establish a closed-loop system interconnection of the identified  $G(s)$  and the parametric transfer matrix  $T_{\text{des}}(s, \alpha)$  as in Fig. 4, where we optimize for the vector of transfer function parameters  $\alpha^*$  which results in an optimal and stable closed-loop performance of the entire power grid response, while ensuring that grid-code and device-level requirements are reliably satisfied.

To address time-varying grid conditions, these two steps have to be repeated regularly, e.g., in a quarterly or hourly fashion when the grid operating point is changing according to the day-ahead market [19]. Of course, also other (event-triggered or periodic)

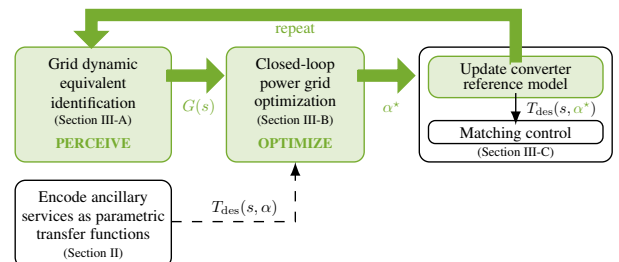


Figure 5: Flowchart of the proposed “*perceive-and-optimize*” (P&O) approach for optimal dynamic ancillary services provision based on power grid perception. The main steps are described in Sections II and III-A to III-C.

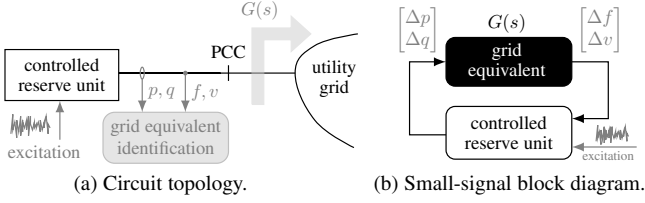


Figure 6: Grid dynamic equivalent identification setup.

repetitions are possible. An investigation of such a multi-cyclic application of the P&O strategy will be part of future work.

### A. Grid Dynamic Equivalent Identification

Since the power grid is ever-changing and usually unknown from the perspective of a generation system, the grid dynamic equivalent  $G(s)$  in (10) has to be measured online for a real-time assessment of the grid dynamics. To do so, for the reserve unit in Fig. 1, we consider a grid-equivalent identification setup as in Fig. 6a, and resort to parametric<sup>1</sup> (i.e., model-based) grid impedance measurement techniques, as in our prior work [20].

To identify  $G(s)$  in (10), we inject uncorrelated wideband excitation signals with small perturbation levels (e.g., random binary sequences (RBS)) in the converter's control loop of the reserve unit, to locally excite the system during online operation as in Fig. 6a (see Section IV for details on the converter control setup). The resulting frequency and voltage magnitude responses, as well as the active and reactive power injections at the PCC, are then measured and collected as discrete-time samples to calculate an estimate of the grid dynamic equivalent  $G(s)$ . Fig. 6b shows a block diagram of the identification problem, where the input/output perspective of the to-be-identified grid equivalent results from the electrical circuit equations.

Given the collected input/output data, we can apply parametric<sup>1</sup> system identification techniques as in [20] to obtain an accurate estimate of the small-signal grid dynamic equivalent  $G(s)$  (see Section IV for examples). One may alternatively choose to first identify the grid impedance in other coordinates and then transform to polar coordinates as in (10) [21], [22].

**Remark 1.** *If the converter system has a small capacity compared to the power grid, it can only locally identify a “partial” grid equivalent in its vicinity, while the rest of the grid appears as an infinite bus. If so, the converter can only affect the grid dynamics during ancillary services provision in this vicinity.*

### B. Closed-Loop Power Grid Optimization

After identifying the grid dynamic equivalent  $G(s)$ , we now compute the optimal parameter vector  $\alpha^*$  of  $T_{\text{des}}(s, \alpha^*)$  which ensures an optimal and stable closed-loop performance of the interconnected system in Fig. 4.

The  $\alpha^*$  computation for the closed-loop system in Fig. 4 can be recast as a system norm (input-output gain) minimization problem as in Fig. 7, where we select a suitable performance index to be minimized. We translate both the grid dynamic equivalent  $G(s)$  and the parametric transfer function matrix  $T_{\text{des}}(s, \alpha)$  into a state-space system representation<sup>2</sup>, where the

<sup>1</sup>Parametric (i.e., model-based) system identification techniques directly identify an explicit system representation (e.g., a transfer function) and are not to be confused with *parametric* (i.e., parameter-dependent) transfer functions.

<sup>2</sup> $T_{\text{des}}(s, \alpha)$  and  $G(s)$  can be ensured to be strictly proper by selecting the transfer function structure during grid-code translation & system identification.

control input of the former is given by the outputs of the latter (i.e., the active and reactive power deviations  $\Delta p$  and  $\Delta q$ ). Moreover, to specify the closed-loop response behavior, we define a weighted performance output  $z_p$  that has to be minimized when subject to some active and reactive power disturbance  $w := [p_d, q_d]^T$ . Namely, we consider  $z_p$  to be composed of the frequency deviation  $\Delta f$ , the rate-of-change-of-frequency (RoCoF)  $\Delta \dot{f}$ , and the voltage deviation  $\Delta v$ , i.e.,

$$z_p = \left( r_f^{\frac{1}{2}} \Delta \dot{f}, r_f^{\frac{1}{2}} \Delta f, r_v^{\frac{1}{2}} \Delta v \right)^T, \quad (11)$$

where  $r_f, r_f, r_v$  are non-negative scalars trading off the relative deviations. If desired, further quantities of the closed-loop interconnection can be added to the performance output  $z_p$ , e.g., the control efforts  $\Delta p$  and  $\Delta q$ . Since the latter, however, are already implicitly limited by the structural constraints on the parameter  $\alpha$ , we refrain from including them into  $z_p$ .

There exist different system norms (e.g.,  $\mathcal{H}_2$  or  $\mathcal{H}_\infty$ ) which provide a measure of the magnitude of the closed-loop system output  $z_p$  in response to the disturbance input  $w$ . In this work, we quantify the closed-loop system performance in terms of the  $\mathcal{H}_2$  norm, which results in a computationally tractable and well-understood design problem, even for complex and large systems. Moreover, the  $\mathcal{H}_2$  norm is generally considered a suitable proxy for typical power system specifications [7]–[9], [23]. In particular, given that the  $\mathcal{H}_2$  norm measures the energy of the system response to impulse disturbance inputs, we can replicate the closed-loop power system response to classical step disturbances, e.g., a sudden load increase or a generation drop, by considering the integral<sup>3</sup> of the performance output in (11) as  $\tilde{z}_p \approx \int z_p$  which, in the  $\mathcal{H}_2$  norm, now reflects the system energy imbalance for *step-like* disturbances. Consequently, we define the cost function as

$$J = \int_0^\infty \tilde{z}_p^T \tilde{z}_p, \quad (12)$$

which corresponds to the squared  $\mathcal{H}_2$  norm between the disturbance input  $w$  and the performance output  $\tilde{z}_p$ .

The underlying dynamical system  $\tilde{z}_p = \tilde{T}_{\text{cl}}(s, \alpha)w$  can be obtained by closing the loop between the two interconnected state-space systems in Fig. 7 and using the integral of (11) as

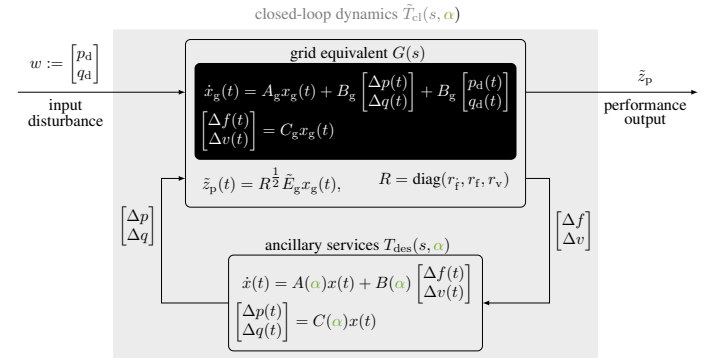


Figure 7: Closed-loop interconnection for  $\mathcal{H}_2$  optimization. The state vector  $x_g$  results from an extended state-space representation of the grid dynamic equivalent, which additionally outputs the approximate integral of  $\Delta f$  and  $\Delta v$ .

<sup>3</sup>Notice that we consider an *approximate* integral of the performance output  $z_p = T_{\text{cl}}(s, \alpha)w$  as  $\tilde{z}_p = \tilde{T}_{\text{cl}}(s, \alpha)w = \frac{1}{s+\epsilon} T_{\text{cl}}(s, \alpha)w$ , where  $\epsilon$  denotes a small approximation factor of an ideal integrator, to ensure that the stability of  $\tilde{T}_{\text{cl}}(s, \alpha)$  and the  $\mathcal{H}_2$  norm are well-defined [24].

$$\begin{aligned} \underbrace{\begin{bmatrix} \dot{x}_g \\ \dot{x}_{cl} \end{bmatrix}}_{\dot{x}_{cl}} &= \underbrace{\begin{bmatrix} A_g & B_g C(\alpha) \\ B(\alpha) C_g & A(\alpha) \end{bmatrix}}_{=:A_{cl}(\alpha)} \underbrace{\begin{bmatrix} x_g \\ x \end{bmatrix}}_{=:x_{cl}} + \underbrace{\begin{bmatrix} B_g \\ O \end{bmatrix}}_{=:B_{cl}(\alpha)} w \\ \tilde{z}_p &= \underbrace{\begin{bmatrix} R^{\frac{1}{2}} \tilde{E}_g & O \end{bmatrix}}_{=:C_{cl}(\alpha)} \underbrace{\begin{bmatrix} x_g \\ x \end{bmatrix}}_{x_{cl}}, \end{aligned} \quad (13)$$

where the state vector  $x_g$  results from an extended state-space representation of the grid dynamic equivalent, which additionally outputs the approximate integral of  $\Delta f$  and  $\Delta v$ .

Finally, by recalling the constraints on  $\alpha$  in (5), (6), (8) and (9), we can state the optimization problem to be solved for  $\alpha^*$  as

$$\begin{aligned} &\underset{\alpha}{\text{minimize}} && J \\ &\text{subject to} && \dot{x}_{cl} = A_{cl}(\alpha)x_{cl} + B_{cl}(\alpha)w \\ & && \tilde{z}_p = C_{cl}(\alpha)x_{cl} \\ & && \alpha \in \mathcal{G} \cap \mathcal{D}, \end{aligned} \quad (14)$$

where  $\mathcal{G} := \mathcal{G}^{\text{fcr}} \times \mathcal{G}^{\text{ffr}} \times \mathcal{G}^{\text{aux}} \times \mathcal{G}^{\text{vq}}$  and  $\mathcal{D} := [[\mathcal{D}^{\text{fcr}} \times \mathcal{D}^{\text{ffr}} \times \mathcal{D}^{\text{aux}}] \cap \mathcal{D}^{\text{fp}}] \times \mathcal{D}^{\text{vq}}$ . Due to the parametric nature of  $A_{cl}(\alpha)$ ,  $B_{cl}(\alpha)$  and  $C_{cl}(\alpha)$ , the problem in (14) is generally non-convex. However, since the objective function is smooth, an explicit gradient of  $J$  can be derived and directly used to solve the optimization problem via scalable first-order methods (e.g., projected gradient descent), similar as in [7]–[9], [23]. A detailed computational approach to derive an expression for the gradient of  $J$  is presented in the appendix.

### C. Realization in Converter Control Architecture

The obtained desired transfer function matrix  $T_{\text{des}}(s, \alpha^*)$  defines a frequency and voltage control behavior in the frequency domain which can be realized in a converter-based generation system. More specifically,  $T_{\text{des}}(s, \alpha^*)$  can be incorporated as a *reference model* into conventional cascaded converter control architectures which are designed for reference tracking, and thus enable a simple matching control implementation, e.g., via classical PI controllers (see Section IV-B for a detailed implementation). Moreover, such an implementation can handle changing reference models  $T_{\text{des}}(s, \alpha^*)$  for different grid conditions with sufficient accuracy, such that a re-tuning of the PI gains is only needed in exceptional cases. Nevertheless, if one desires more advanced and robust matching control implementations, one could alternatively resort to multivariable linear parameter varying (LPV)  $\mathcal{H}_\infty$  methods [15], [25], which can robustly include the time-varying parameter vector  $\alpha$ , and hence directly account for time-varying grid conditions without re-computing the matching controller. However, the high-dimensionality and non-linear dependency of the parameters in  $T_{\text{des}}(s, \alpha^*)$  might lack practical realizability of LPV methods.

Beyond that, instead of realizing  $T_{\text{des}}(s, \alpha^*)$  with one single reserve unit, one might alternatively consider a heterogeneous collection of multiple energy sources (i.e., a so-called dynamic virtual power plant (DVPP)) to provide  $T_{\text{des}}(s, \alpha^*)$  in aggregation [15], [25]. This offers the advantage of providing dynamic ancillary services via  $T_{\text{des}}(s, \alpha^*)$  across higher energy and power levels and a wider range of time-scales, even during time-varying conditions of individual energy sources.

## IV. CASE STUDIES

To demonstrate the effectiveness of the proposed P&O approach, we use Simscape Electrical in MATLAB/Simulink to perform a detailed electromagnetic transients (EMT) simulation based on a *nonlinear* model of the three-phase two-area test system in Fig. 8. In a first case study, we investigate how one single reserve unit, after applying the P&O strategy, can significantly improve the overall closed-loop power grid performance during nominal grid conditions, while satisfying grid-code and device-level requirements. In a second case study, we consider oscillatory grid conditions caused by weakly-damped inter-area modes, and reveal how a sequential application of the P&O strategy by multiple reserve units allows us to iteratively optimize the overall frequency and voltage response behavior of the power grid while attenuating the inter-area oscillations.

### A. Two-Area Test System Model

The two-area system in Fig. 8 consists of two areas connected by a weak tie. It contains four thermal-based synchronous generators (SGs) and two additional converter-based reserve units connected to buses 12 and 13. The transmission lines are modeled via nominal  $\pi$  sections (i.e., with RLC dynamics), and the step-up transformers via three-phase linear models. We adopt an 8th-order model for the synchronous machines equipped with an IEEE type 1 voltage regulator (AVR) combined with an exciter, and a power system stabilizer (PSS). The governors are modeled as a proportional speed-droop control with first-order delay, and the turbines as reheat steam turbines [26]. The power grid parameters are chosen similarly as in [26], and the main parameters of the SGs are summarized in Table II.

### B. Converter-Interfaced Generation System

The proposed grid-side converter model is shown in Fig. 9 with the associated parameters in Table III. It represents an aggregation of multiple commercial converter modules and is based on a state-of-the-art converter control scheme [27]. We can easily incorporate the required grid dynamic equivalent identification setup and the transfer-function matching control in such a setting. While Fig. 9 shows only one exemplary converter control architecture, our method is compatible with any control architecture that accepts active and reactive power references.

Similar to [28], we assume the dc current  $i_{dc}$  to be supplied by a controllable dc current source, e.g., schematically representing the machine-side converter of a direct-drive wind turbine, a PV system, etc. In particular, we consider a generic coarse-grain model of the primary source and model its response time by a first-order delay with a time constant  $\tau_{dc}$  [28], e.g., representing the dynamics of the resource as well as communication and/or actuation delays. Further, we limit the primary source

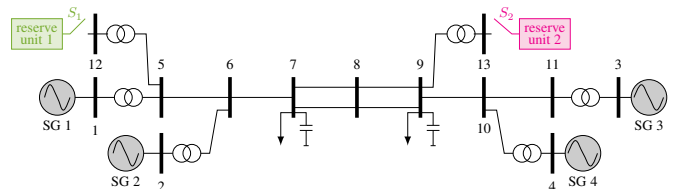


Figure 8: One-line diagram of the three-phase two-area test system with two converter-based reserve units for optimal dynamic ancillary services provision.

Table II: Main parameters of the SGs in the nominal two-area system.

Parameter	Value	Parameter	Value
SG power rating	900 MVA	Exciter gain	200
SG voltage rating	20 kV	Exciter time const.	0.001 s
Governor droop gain	0.05	PSS gain	25
Governor time constant	0.2 s	PSS wash-out time const.	1 s
Steam chest time constant	0.5 s	Lead-lag time const. # 1	50e-3 s, 20e-3 s
Turbine power fraction	0.3	Lead-lag time const. # 2	3 s, 5.4 s
Reheat time constant	8 s	Equivalent inertia	4 s (SG 1&2) 4.35 s (SG 3&4)

input by a saturation element, which, e.g., corresponds to the power/current limits of a machine-side converter or an energy storage system, or PV/wind power generation limits. For wind or PV generation, we assume that they are operated under deloaded conditions with respect to their maximum power point, allowing them to put an active power reserve aside for participating in frequency regulation. While we stick to such an abstract representation of the primary source, one could also consider more detailed models tailored to the application at hand.

The ac-side control of the grid-side converter is used to control the output current magnitude. It is implemented in a dq-coordinate frame generated via a phase-locked loop (PLL), which tracks the system frequency to keep the converter synchronized with the grid voltage [27].

To identify the grid dynamic equivalent  $G(s)$ , we inject uncorrelated wideband excitation signals with small perturbation levels in the converter's control loop to excite the power grid during online operation as indicated in Fig. 9. The resulting frequency and voltage magnitude responses, as well as the active and reactive power injections at the PCC are then measured and collected in the form of discrete-time samples to calculate an estimate of the grid dynamic equivalent  $G(s)$ .

Finally, the transfer function matching control is included in the outer control loop of the converter via simple PI controllers to track the desired dynamic response behavior for frequency and voltage regulation as  $T_{des}^{fp}(s, \alpha^*)$  and  $T_{des}^{vq}(s, \alpha^*)$ , respectively.

### C. Benchmark Ancillary Services Specification

To demonstrate the efficiency of the proposed P&O strategy in the following case studies, we define a *cheap* desired transfer function matrix  $T_{des}(s, \alpha_0)$  as a benchmark ancillary services specification to compare with. More specifically, we select  $\alpha_0$  as the critical point within  $\mathcal{G}$  where all grid-code constraints in (5), (6), (8) and (9) are active, i.e.,

$$\begin{aligned}
 \text{FCR: } & t_i^{fcr} = t_{i,max}^{fcr}, \quad t_a^{fcr} = t_{a,max}^{fcr} \\
 \text{FFR: } & t_a^{ffr} = t_{a,max}^{ffr}, \quad t_d^{ffr} = t_{d,min}^{ffr}, \quad t_r^{ffr} = t_{r,min}^{ffr}, \quad x^{ffr} = 1 \\
 \text{AUX: } & m_{aux} = 0 \\
 \text{VQ: } & t_{90}^{vq} = t_{90,max}^{vq}, \quad t_{100}^{vq} = t_{100,max}^{vq}
 \end{aligned} \tag{15}$$

thereby encoding the *minimum* open-loop grid-code requirements as in Table Ia. In particular, such a basic choice of  $\alpha_0$  results in a cheap, but feasible dynamic ancillary services provision, where the effort of the reserve unit is pared down to the minimum. The active and reactive power responses of the cheap control  $T_{des}(s, \alpha_0)$  (and the underlying piece-wise linear time-domain curves) after a frequency and voltage step change are depicted in Fig. 10. The associated active and reactive power capacity levels are fixed by the allocated active and reactive power droop gains  $D_p = -0.05$ ,  $K_p = -0.04$  and

Table III: Converter parameters of reserve units 1 and 2.

Parameter	Symbol	Value
Voltage, power & frequency base	$V_b, S_b, f_b$	1 kV, 500 MVA, 50 Hz
DC-link capacitor	$C_{dc}$	0.24 p.u.
RL-filter components	$L_f, R_f$	0.1 p.u., 0.01 p.u.
DC-source time constants	$\tau_{dc,1}, \tau_{dc,2}$	0.1 s, 0.04 s
Norm. max. active power ramp. rate	$R_{max,1}^p, R_{max,2}^p$	111 p.u./s, 150 p.u./s
Norm. max. reactive power ramp. rate	$R_{max,1}^q, R_{max,2}^q$	150 p.u./s, 150 p.u./s
Norm. max. active power peak capac.	$M_{max,1}^p, M_{max,2}^p$	70 p.u., 100 p.u.
Max. FFR support duration	$t_{d,max,1}^{ffr}, t_{d,max,2}^{ffr}$	20 s, 20 s
Max. return-to-recovery time	$t_{r,max,1}^{ffr}, t_{r,max,2}^{ffr}$	20 s, 20 s

\*Indices 1 and 2 refer to reserve units 1 and 2, respectively. No index implies identical values for reserve units 1 and 2.

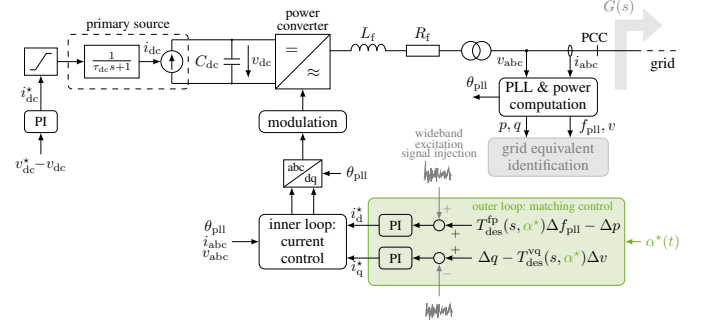
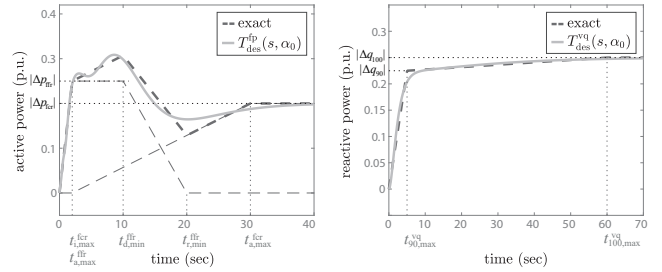


Figure 9: One-line diagram of three-phase power converter interface of one reserve unit including grid equivalent identification and matching control.

Figure 10: Active and reactive power response after a negative frequency and voltage step change for the cheap  $T_{des}(s, \alpha_0)$  which satisfies minimal grid-code requirements (cf. grid-code examples in Figures 2 and 3).

$D_q = -0.04$  (cf. Figures 2 and 3b). Notice that we will use the same droop gains also for the optimal  $T_{des}(s, \alpha^*)$  computation in the following case studies, since they are typically directly given by the system operator and might not allow for flexibility.

### D. Case Study I: Optimal Ancillary Services Provision During Nominal Grid Conditions

We commence our validation by examining nominal grid conditions, where only reserve unit 1 is interconnected with the two-area system (S1 closed in Fig. 8), while reserve unit 2 remains disconnected (S2 open). As a starting point, we consider the cheap transfer function matrix  $T_{des,1}(s, \alpha_0)$  to be realized in the outer loop of the converter system of reserve unit 1. Based on this, we aim to improve the overall closed-loop power grid performance by applying the P&O strategy to compute an optimal  $T_{des,1}(s, \alpha_{nom}^*)$  for reserve unit 1.

1) *Grid Dynamic Equivalent Identification*: We use the converter interface of reserve unit 1 to identify the grid dynamic equivalent  $G_1(s)$  as in Fig. 11a. During the online grid identification experiment, we consider constant stationary grid conditions. To excite the power grid, we inject two uncorrelated superimposed RBS signals, each with an amplitude of 0.03 p.u. and a sampling rate of 1 kHz, in the power loop of the converter

control architecture in Fig. 9 for 40 seconds. When doing so, we ensure that the perturbation level is rather small to not deteriorate the ongoing grid operation.

The small-signal frequency and voltage magnitude responses, as well as the active and reactive power injections at the PCC of reserve unit 1, are then measured and collected (in the presence of measurement noise) at a sampling rate of 1 kHz. Since the recorded data set is based on discrete-time samples, the parametric grid impedance model is (initially) identified in the discrete domain. Namely, following a similar procedure as in [20], we compute an ARX model by applying parametric system identification techniques. We additionally include other processing steps (e.g., prefiltering of the data) to ensure the accuracy of the system identification in the frequency range of interest. A proper model structure and order selection is done iteratively by testing a certain model structure and order and checking the fitting performance with some validation data. Once an appropriate ARX transfer function model has been identified, we apply model reduction techniques and convert it from discrete into continuous domain to finally obtain  $G_1(s)$  of order 17. The resulting Bode diagram of  $G_1(s)$  is illustrated by the solid green line in Fig. 12. We can see that an accurate fitting of the reference grid model (obtained via sinusoidal sweep methods and indicated by the star symbols) is obtained.

2) *Optimal  $T_{des}$  Computation*: Once the dynamic grid equivalent  $G_1(s)$  is identified, we proceed to solve the closed-loop power grid optimization problem as detailed in Section III-B, to compute a locally optimal solution for  $\alpha_{nom}^*$ , while taking both grid-code and local device-level limitations of reserve unit 1 (see Table III) into consideration. It is crucial to note that  $G_1(s)$  is a full  $2 \times 2$  matrix, therefore capturing the inherent coupling of active and reactive power with both frequency and voltage during closed-loop optimization. The resulting optimal parameter vector  $\alpha_{nom}^*$  is presented in Table IV. A comparative analysis of the open-loop step response behaviors of the optimal  $T_{des,1}(s, \alpha_{nom}^*)$  and the cheap  $T_{des,1}(s, \alpha_0)$  in Fig. 13 allows us to conclusively assess the reliable satisfaction of minimum grid-code requirements of  $T_{des,1}(s, \alpha_{nom}^*)$ . Finally, by realizing the obtained  $T_{des,1}(s, \alpha_{nom}^*)$  in the converter control loop of reserve unit 1, we observe a significant enhancement of the closed-loop system response behavior. Namely, despite being bandwidth and capacity-limited, and with only half the rating of one SG, the optimal dynamic ancillary services provision by reserve unit 1 demonstrates a substantial improvement of the system response during a load increase at bus 7 (Fig. 14). Specifically, we achieve a **12.6%** improvement in RoCoF, an **11.6%** improvement in frequency nadir, and a **32.9%** reduction in voltage peak compared to the initial cheap  $T_{des,1}(s, \alpha_0)$

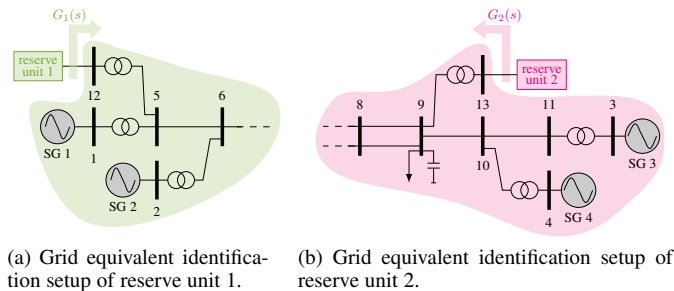


Figure 11: Grid dynamic equivalent identification of the two-area system.

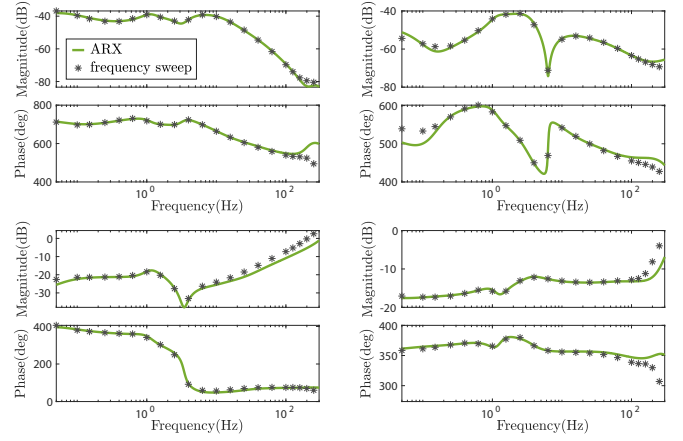


Figure 12: Bode diagrams of the identified  $2 \times 2$  grid dynamic equivalent  $G_1(s)$  for the nominal two-area system in Fig. 11a.

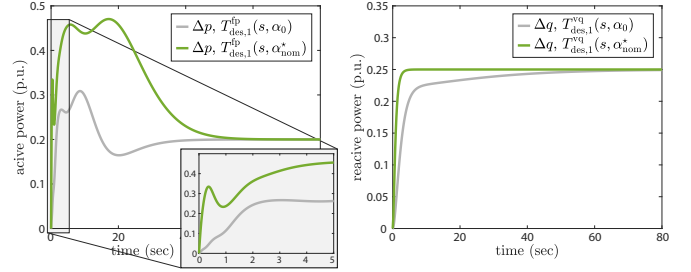


Figure 13: Open-loop active and reactive power step responses after a negative frequency and voltage step change for the optimal  $T_{des,1}(s, \alpha_{nom}^*)$  and the cheap  $T_{des,1}(s, \alpha_0)$ , respectively.

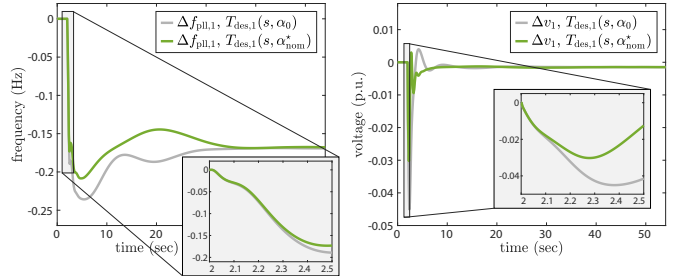


Figure 14: Closed-loop system response behavior of the nominal two-area system after a load increase at bus 7 for the optimal  $T_{des,1}(s, \alpha_{nom}^*)$  and the cheap  $T_{des,1}(s, \alpha_0)$ , respectively.

implementation.

### E. Case Study II: Optimal Ancillary Services Provision During Oscillatory Grid Conditions with Multiple Reserve Units

We now consider oscillatory grid conditions caused by weakly-damped inter-area modes, arising from long transmission lines, fast exciters, and ill-tuned PSS gains (we decreased the PSS gains by a factor of five). Both reserve units are connected to the 2-area system (S1 and S2 closed), initially providing ancillary services as specified by the cheap transfer function matrices  $T_{des,1}(s, \alpha_0)$  and  $T_{des,2}(s, \alpha_0)$ , respectively. Being limited in energy, reserve unit 2, does not provide the FCR service, i.e., we eliminate the  $T_{des,2}^{fcr}$  term in (3).

Similar to the state-of-the-art practice of grid impedance identification, which is based on independent identification procedures of each converter unit, we study a multi-converter scenario of the proposed method for optimal dynamic ancillary services provision, where each reserve unit applies the P&O



Table IV: Optimal transfer function parameters  $\alpha^*$  for case studies I and II.

	$t_{i1}^{fcr}$	$t_{a1}^{fcr}$	$t_{d1}^{fcr}$	$t_{r1}^{fcr}$	$x_{fcr}$	$\omega_1$	$\omega_h$	$m_{aux}$	$t_{90}^{vq}$	$t_{100}^{vq}$
$\alpha_0$	2	30	2	10	20	1	-	0	5	60
$\alpha_{nom}^*$	0.01	3.73	1.32	21.32	41.32	1	2.4	7	-43.15	2.87
$\alpha_{osci}^* \#1$	0.01	5.64	1.65	21.65	41.65	1	5.36	9.96	-40.16	0.29
$\alpha_{osci}^* \#2$	-	-	0.84	20.84	40.84	1.35	0.95	5.55	-64	0.48

strategy sequentially one after another, while the remaining units stay connected with their previous  $T_{des,i}(s, \alpha^*)$ .

1) *First P&O Cycle*: During grid identification, we obtain  $G_1(s)$  of order 20. The resulting Bode diagram is illustrated by the solid green line in Fig. 15, with a significant resonance peak at approximately 1 Hz, indicating the oscillation frequency of the weakly-damped inter-area modes of the two-area system.

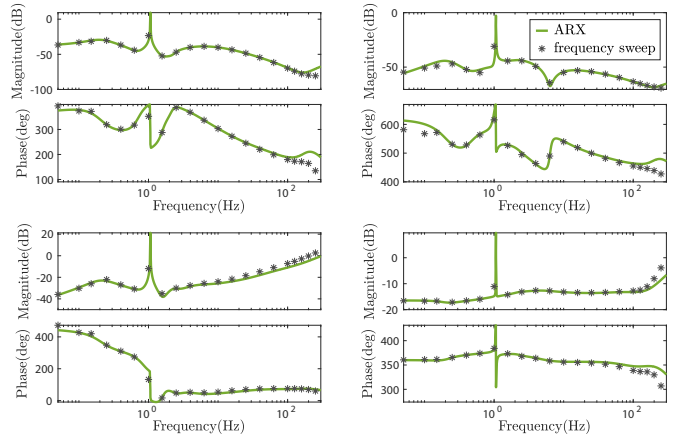
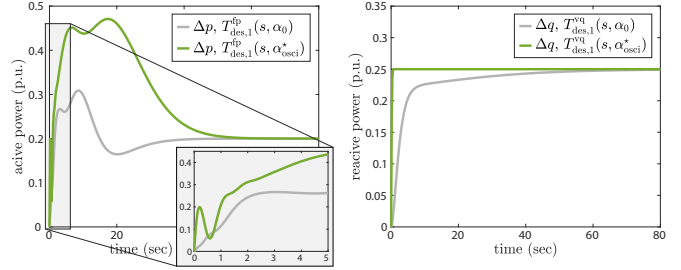
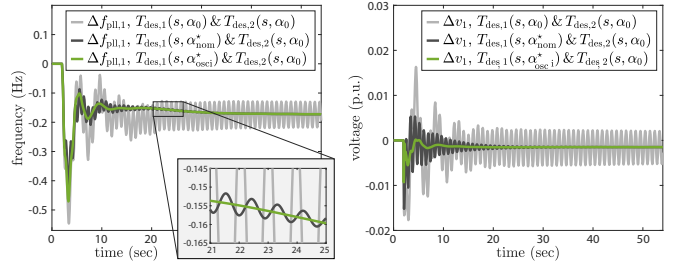
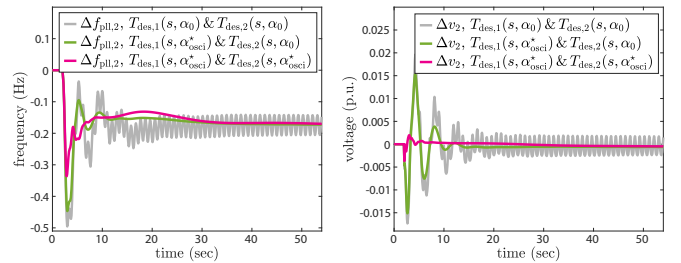
For identical cost-function weights and gradient descent algorithm settings as in case study I, we compute an optimal  $\alpha_{osci}^*$  as listed in Table IV. The associated open-loop step response of  $T_{des,1}(s, \alpha_{osci}^*)$  is depicted in Fig. 16. By comparing  $\alpha_{osci}^*$  with the optimal  $\alpha_{nom}^*$  from the previous case study I during nominal grid conditions, it becomes apparent how different grid conditions generally result in a different optimal dynamic ancillary services provision (for the same optimization settings).

With  $T_{des,1}(s, \alpha_{osci}^*)$ , we can improve the oscillatory closed-loop system response of the two-area system quite significantly, i.e., once again, the performance enhancement of  $\alpha_{osci}^*$  over  $\alpha_0$  is astonishing. As illustrated in Fig. 17, the inter-area oscillations at 1 Hz are significantly attenuated during a load increase at bus 7. Moreover, compared to the system response with the cheap  $T_{des,1}(s, \alpha_0)$ , we can achieve a **10.5%** improvement in RoCoF, a **13.8%** improvement in frequency nadir, and a voltage peak reduction of **47.5%**. Finally, the optimal  $T_{des,1}(s, \alpha_{osci}^*)$  for nominal grid conditions in case study I does not result in a satisfying response behavior when deployed in the oscillatory grid, which justifies the necessity of perceiving the grid characteristics in an online manner during changing grid conditions.

2) *Second P&O Cycle*: Keeping  $T_{des,1}(s, \alpha_{osci}^*)$  for reserve unit 1, we now apply the P&O strategy to reserve unit 2. After a grid identification as in Fig. 11b, we obtain  $G_2(s)$  of order 24 and compute the optimal  $T_{des,2}(s, \alpha_{osci}^*)$  with  $\alpha_{osci}^*$  as in Table IV. Compared to the first P&O cycle, we can clearly observe a further improvement of the overall closed-loop grid response behavior during a load increase at bus 7 (Fig. 18), i.e., a RoCoF improvement of **16.1%**, a frequency nadir improvement of **24.7%**, and a voltage peak improvement of **75.9%**.

## V. CONCLUSION

We have presented a systematic approach to provide optimal dynamic ancillary services with converter-interfaced generation systems based on local power grid perception. To do so, we used the “*perceive-and-optimize*” (P&O) strategy: We first identified a grid dynamic equivalent at the interconnection terminals of the converter, and then established a closed-loop system interconnection of the identified grid equivalent and a desired transfer function matrix, where we optimize for the latter to provide optimal dynamic ancillary services. In the process, we ensure that grid-code and device-level requirements are satisfied. Our numerical experiments verify the superiority of our approach over cheap ancillary services provision based on minimum (open-loop) grid-code requirements, especially during changing grid-conditions.

Figure 15: Bode diagrams of the identified  $2 \times 2$  grid dynamic equivalent  $G_1(s)$  for the oscillatory two-area system in Fig. 11a during the first P&O cycle.Figure 16: Open-loop active and reactive power step responses after a negative frequency and voltage step change for the optimal  $T_{des,1}(s, \alpha_{osci}^*)$  and the cheap  $T_{des,1}(s, \alpha_0)$ , respectively.Figure 17: Closed-loop system response behavior of the oscillatory two-area system after a load increase at bus 7. We compare the optimal  $T_{des,1}(s, \alpha_{osci}^*)$ , the nominal  $T_{des,1}(s, \alpha_{nom}^*)$ , and the cheap  $T_{des,1}(s, \alpha_0)$ , of reserve unit 1, respectively. Reserve unit 2 is always realizing the cheap  $T_{des,2}(s, \alpha_0)$ .Figure 18: Closed-loop system response behavior of the oscillatory two-area system after a load increase at bus 7. We compare the initial system configuration based on the cheap  $T_{des,1}(s, \alpha_0)$  and  $T_{des,2}(s, \alpha_0)$  of both units, with the optimal  $T_{des,1}(s, \alpha_{osci}^*)$  of unit 1 after the first P&O cycle and the optimal  $T_{des,2}(s, \alpha_{osci}^*)$  of unit 2 after the second P&O cycle.

Future work should address how to incentivize our concept by future ancillary services markets or tender-based contract requirements for grid connection [29], [30]. Namely, already now, first attempts on how to assimilate novel high-performing dynamic ancillary service products into future markets have been proposed [29]–[31]. Moreover, our results might inspire

the formulation of next-generation grid codes (e.g., in the frequency domain, as closed-loop specifications, by respecting local conditions, considering grid-forming requirements, etc.).

## VI. APPENDIX: $\mathcal{H}_2$ OPTIMIZATION

The  $\mathcal{H}_2$ -norm between the disturbance input  $w$  and the performance output  $\tilde{z}_p$  of the system in (13) is given by [24]

$$\begin{aligned} J &= \|\tilde{T}_{cl}(s, \alpha)\|_2^2 \\ &= \text{trace}(C_{cl}(\alpha)PC_{cl}(\alpha)^\top) \\ &= \text{trace}(B_{cl}(\alpha)^\top QB_{cl}(\alpha)), \end{aligned} \quad (16)$$

where  $P$  and  $Q$  are the observability and controllability Gramain obtained as the positive definite solutions of the Lyapunov equation and its dual

$$A_{cl}(\alpha)P + PA_{cl}(\alpha)^\top + B_{cl}(\alpha)B_{cl}(\alpha)^\top = 0 \quad (17a)$$

$$A_{cl}(\alpha)^\top Q + QA_{cl}(\alpha) + C_{cl}(\alpha)^\top C_{cl}(\alpha) = 0, \quad (17b)$$

parameterized in  $\alpha$  for the given closed-loop system matrices  $A_{cl}(\alpha)$ ,  $B_{cl}(\alpha)$  and  $C_{cl}(\alpha)$ . Based on the latter, the optimization problem in (14) to compute the locally optimal  $\alpha^*$  with respect to the  $\mathcal{H}_2$  norm  $\|\tilde{T}_{cl}(s, \alpha)\|_2^2$  can be recasted as

$$\begin{aligned} &\underset{\alpha, P, Q}{\text{minimize}} \quad \text{trace}(C_{cl}(\alpha)PC_{cl}(\alpha)^\top) \\ &\text{subject to} \quad \alpha \in \mathcal{G} \cap \mathcal{D}, \quad (17), \quad P \succ 0, \quad Q \succ 0. \end{aligned} \quad (18)$$

The constraints (17) make the problem (18) non-convex and difficult to solve. However, since the objective function is smooth, an explicit gradient  $\nabla_\alpha J = \nabla_\alpha \text{trace}(C_{cl}(\alpha)PC_{cl}(\alpha)^\top)$  can be derived and directly used to solve (18) for the (locally) optimal parameter vector  $\alpha^*$  via scalable first-order methods such as projected gradient descent (or variants and metaheuristics thereof [32]). In particular, using steps similar to the ones in [8], the gradient with respect to the vector  $\alpha$  can be computed as

$$\nabla_\alpha J = \left[ \frac{\partial J}{\partial \alpha_1}, \frac{\partial J}{\partial \alpha_2}, \dots, \frac{\partial J}{\partial \alpha_n} \right]^\top, \quad (19)$$

where each component  $\frac{\partial J}{\partial \alpha_i}$  is given as

$$\frac{\partial J}{\partial \alpha_i} = 2 \cdot \text{trace} \left( \frac{\partial A_{cl}}{\partial \alpha_i} P Q \right) + \text{trace} \left( \frac{\partial (B_{cl} B_{cl}^\top)}{\partial \alpha_i} Q \right) + \text{trace} \left( P \frac{\partial (C_{cl}^\top C_{cl})}{\partial \alpha_i} \right).$$

## VII. ACKNOWLEDGEMENTS

The authors wish to thank Simon Wenig from Mosaic Grid Solutions GmbH for his fruitful comments and discussions.

## REFERENCES

- [1] E. Commission, "Commission regulation (EU) 2016/631 of 14 april 2016, establishing a network code on requirements for grid connection of generators," *Off. J. Eur. Union*, 2016.
- [2] F. Oyj, "The technical requirements and the prequalification process of frequency containment reserves (FCR)," 2021.
- [3] EirGrid, "DS3 system services agreement," 2018.
- [4] N. Modig, R. Eriksson, L. Haarla, P. Ruokolainen, M. Kuivaniemi, K. Hornnes, P. Vada, S. Meybodi, and D. Karlsson, "Technical requirements for fast frequency reserve provision in the nordic synchronous area," *ENTSO-E*, 2019.
- [5] H. Geng, X. Xi, and G. Yang, "Small-signal stability of power system integrated with ancillary-controlled large-scale DFIG-based wind farm," *IET Renewable Power Generation*, vol. 11, no. 8, pp. 1191–1198, 2017.
- [6] J. Ying, X. Yuan, J. Hu, and W. He, "Impact of inertia control of DFIG-based wt on electromechanical oscillation damping of sg," *IEEE Trans. Power Syst.*, vol. 33, no. 3, pp. 3450–3459, 2018.

- [7] B. K. Poolla, D. Groß, and F. Dörfler, "Placement and implementation of grid-forming and grid-following virtual inertia and fast frequency response," *IEEE Trans. Power Syst.*, vol. 34, no. 4, pp. 3035–3046, 2019.
- [8] A. Ademola-Idowu and B. Zhang, "Optimal design of virtual inertia and damping coefficients for virtual synchronous machines," in *2018 IEEE Power & Energy Society General Meeting (PESGM)*, pp. 1–5.
- [9] D. Groß, S. Bolognani, B. K. Poolla, and F. Dörfler, "Increasing the resilience of low-inertia power systems by virtual inertia and damping," in *Proceedings of IREP'2017 Symposium*. International Institute of Research and Education in Power System Dynamics ..., 2017, p. 64.
- [10] L. Ruttledge and D. Flynn, "Emulated inertial response from wind turbines: gain scheduling and resource coordination," *IEEE Trans. Power Syst.*, vol. 31, no. 5, pp. 3747–3755, 2015.
- [11] Z. Wu, W. Gao, T. Gao, W. Yan, H. Zhang, S. Yan, and X. Wang, "State-of-the-art review on frequency response of wind power plants in power systems," *Journal of Modern Power Systems and Clean Energy*, vol. 6, no. 1, pp. 1–16, 2018.
- [12] K. Clark, N. W. Miller, and J. J. Sanchez-Gasca, "Modeling of GE wind turbine-generators for grid studies," *GE energy*, vol. 4, pp. 0885–8950, 2010.
- [13] C. Roberts, D. Arnold, and D. S. Callaway, "An online adaptive damping controller for converter-interfaced generation," *IEEE Trans. Power Syst.*, 2023.
- [14] K. De Brabandere, B. Bolsens, J. V. d. Keybus, A. Woyte, J. Driesen, and R. Belmans, "A voltage and frequency droop control method for parallel inverters," *IEEE Trans. Power Electron.*, vol. 22, no. 4, pp. 1107–1115, 2007.
- [15] V. Häberle, A. Tayyebi, X. He, E. Prieto-Araujo, and F. Dörfler, "Grid-forming and spatially distributed control design of dynamic virtual power plants," *IEEE Trans. Smart Grid*, 2023.
- [16] "Analysis of the synchronisation capabilities of BESS power converters," OSMOSE, European Union Horizon 2020 research and innovation program, Tech. Rep., 2022.
- [17] E. de España, "Norma técnica de supervisión de la conformidad de los módulos de generación de electricidad según el reglamento ue 2016/631: Tech. rep," 2021.
- [18] V. Häberle, L. Huang, X. He, E. Prieto-Araujo, and F. Dörfler, "Dynamic ancillary services: From grid codes to transfer function-based converter control," *arXiv:2310.01552*, 2023.
- [19] D. S. Kirschen and G. Strbac, *Fundamentals of power system economics*. John Wiley & Sons, 2018.
- [20] V. Häberle, L. Huang, X. He, E. Prieto-Araujo, R. S. Smith, and F. Dörfler, "MIMO grid impedance identification of three-phase power systems: Parametric vs. nonparametric approaches," *arXiv:2305.00192*, 2023.
- [21] Z. Yang, C. Mei, S. Cheng, and M. Zhan, "Comparison of impedance model and amplitude-phase model for power-electronics-based power system," *IEEE Journal of Emerging and Selected Topics in Power Electronics*, vol. 8, no. 3, pp. 2546–2558, 2019.
- [22] X. Wang, L. Harnefors, and F. Blaabjerg, "Unified impedance model of grid-connected voltage-source converters," *IEEE Trans. Power Electron.*, vol. 33, no. 2, pp. 1775–1787, 2017.
- [23] E. Sanchez-Sanchez, D. Gross, E. Prieto-Araujo, F. Dörfler, and O. Gomis-Bellmunt, "Optimal multivariable mmc energy-based control for dc voltage regulation in hvdc applications," *IEEE Trans. Power Del.*, vol. 35, no. 2, pp. 999–1009, 2019.
- [24] K. Zhou, J. Doyle, and K. Glover, *Robust and optimal control*. Prentice hall, 1996.
- [25] V. Häberle, M. W. Fisher, E. Prieto-Araujo, and F. Dörfler, "Control design of dynamic virtual power plants: An adaptive divide-and-conquer approach," *IEEE Trans. Power Syst.*, vol. 37, no. 5, pp. 4040–4053, 2021.
- [26] P. Kundur, "Power system stability," *Power System Stability and Control*, pp. 7–1, 2007.
- [27] A. Yazdani and R. Iravani, *Voltage-sourced converters in power systems*. Wiley Online Library, 2010, vol. 39.
- [28] A. Tayyebi, D. Groß, A. Anta, F. Kupzog, and F. Dörfler, "Frequency stability of synchronous machines and grid-forming power converters," *IEEE Trans. Emerg. Sel. Topics Power Electron.*, vol. 8, no. 2, pp. 1004–1018, 2020.
- [29] D. Fernández-Muñoz, J. I. Pérez-Díaz, I. Guisández, M. Chazarra, and A. Fernández-Espina, "Fast frequency control ancillary services: An international review," *Renewable and Sustainable Energy Reviews*, vol. 120, p. 109662, 2020.
- [30] L. Meng, J. Zafar, S. K. Khadem, A. Collinson, K. C. Murchie, F. Coffele, and G. M. Burt, "Fast frequency response from energy storage systems—a review of grid standards, projects and technical issues," *IEEE Trans. Smart Grid*, vol. 11, no. 2, pp. 1566–1581, 2019.
- [31] C. Feng, L. Huang, X. He, Y. Wang, F. Dörfler, and Q. Chen, "Joint oscillation damping and inertia provision service for converter-interfaced generation," *arXiv:2309.01321*, 2023.
- [32] D. P. Bertsekas, *Nonlinear Programming*. Scientific, Athena, 1999.